J Appl Electrochem (2007) 37:1027–1037
DOI 10.1007/s10800-007-9344-y

ORIGINAL PAPER

Characterisation of porous and barrier layers of anodic oxides on different aluminium alloys

S. Feliu Jr. · J. A. González · V. López · M. J. Bartolome · E. Escudero · E. Otero

Received: 18 December 2006 / Revised: 1 June 2007 / Accepted: 7 June 2007 / Published online: 29 June 2007

Abstract Electrochemical impedance spectroscopy (EIS) provides a powerful tool for obtaining detailed information on the electrochemical properties of both porous and barrier layers on different aluminium alloys. The impedance value at a given frequency can serve to calculate the electrochemical parameters of the oxide layers represented by each component of the equivalent circuit (EC) which reproduces the behaviour of the studied systems. It is thus possible, with these parameters, to analyse the effects of any factor on the sealing and ageing processes of anodic aluminium oxide layers. Electrochemical results are completed with a detailed analytical study of the oxide layers by XPS, with gravimetric determinations of the changes experienced in the anodising and sealing processes, and with microstructural characterisation of the anodic films by scanning electron microscopy (SEM).

Keywords Aluminium alloys · Anodising · Ageing · XPS · EIS

1 Introduction

Aluminium and its alloys are highly reactive materials and to improve their durability in many environments they are often subjected to anodising and sealing processes. In their most important applications—architecture, transport and domestic appliances—anodising is performed in sulphuric acid solutions, giving rise to a porous structure of hexagonal columnar cells, like a honeycomb, each of which consists of a central pore of 100–200 Å in diameter surrounded by alumina walls of 100–200 Å. These cells are normal to the metallic substrate and are separated from it by a barrier layer of a low thickness, around 150 Å [1].

Electrochemical impedance spectroscopy (EIS) [2–10] and transmission electron microscopy (TEM) [10–15] have been shown to be the most suitable techniques for studying aluminium oxide layers and, based essentially on these techniques, the authors have previously performed research on traditional hydrothermal sealing [16–18], cold sealing [18, 19], and the changes experienced by anodic coatings during ageing, a process that remains active for many years [20–24]. The foregoing studies were all carried out using 1050 alloy as the base material; this is aluminium of commercial purity with at least 99.5% Al.

The intention of the present work is to specify the characteristics of the anodic films formed on four substantially different aluminium alloys with the aim of knowing to what point the knowledge acquired with aluminium of commercial purity can be extended to other aluminium alloys. The XPS technique has been used to determine, as the starting point, the composition of the anodic layers. EIS was used to estimate the electrical characteristics of the barrier and porous sublayers and their changes with the sealing and ageing processes, and using SEM an attempt has been made to relate behaviour to microstructural features. Furthermore, by means of simple gravimetry, the efficiency of the anodic layer formation process and the macroscopic characteristics that define layer quality have been estimated.

S. Feliu Jr. (✉) · J. A. González · V. López · M. J. Bartolome · E. Escudero · E. Otero
Centro Nacional de Investigaciones Metalúrgicas, Av. Gregorio del Amo, 8, 28040 Madrid, Spain
e-mail: sfeliu@cenim.csic.es

2 Experimental procedure

2.1 Al alloys

The tested aluminium alloys were 1050 Al of commercial purity, 2017-T4 of Al-4% Cu, 5754-H111 of Al-2.90% Mg and 6082-T6, of Al-0.88% Si-0.80% Mg. The T4 state refers to solution heat treatment followed by natural ageing, T6 refers to solution treating and artificial ageing, and H111 to annealing, with holding, in all cases, at temperatures of more than 300 °C. These alloys are referred to throughout the work as pure Al, Al–Cu, Al–Mg and Al–Si–Mg, respectively. The alloy referred to as pure Al (commercially pure Al) contains a total of about 0.5 wt% of other elements, mainly iron (0.290 wt% Fe) and silicon. Elemental compositions, determined in wet conditions, are detailed in Table 1. Anodized (and sealed) Al–Si–Mg, Al–Mg and commercially pure Al materials are widely used in architectural applications. They present different possibilities regarding the oxidation tendencies of the alloying elements and content and composition of second phase particles in the aluminium matrix. The Al–Cu alloy has the peculiarity of giving very defective oxide coatings [25, 26].

2.2 Anodising of specimens

The $100 \times 50 \times 1.5$ mm specimens were degreased by submerging them for 5 min in an aqueous solution of phosphoric and chromic acids at concentrations of 250 g L^{-1}. and 55 g L^{-1}, respectively, at a temperature of 30–40 °C. They were then etched by chemical attack in an aqueous solution of 100 g L^{-1} sodium hydroxide at 40 °C for variable times, and were desmutted by immersion for a few seconds in the previous mentioned mixture of sulphuric and chromic acids. After each treatment the specimens were thoroughly rinsed in distilled water and dried with compressed air.

Anodic coatings were generated on specimens of the various alloys by submerging them in an aqueous dissolution of 180 g L^{-1} H_2SO_4 at 20 °C stirred with compressed air, through which a direct current density of 1.5 A dm^{-2} was pased. The anodising times were variable, being chosen to produce coatings of approximately 5, 15 and 30 μm. Some specimens were then subjected to traditional hydrothermal sealing in boiling deionised water for 60 min, sufficiently long to achieve the sealing quality indices demanded by industry, even with the thickest coatings.

2.3 XPS technique

Surface analyses of the specimens was carried out using a VG Microtech spectrometer, model MT 500, and an X-ray source with a magnesium anode (radiation energy Kα = 1253.6 eV) operating at a voltage of 15 keV and an emission current of 20 mA (300 W). During the experiment the working pressure in the UHV (Ultra-High Vacuum) system analysis cabinet was held at less than 1×10^{-9} Torr. The spectrometer was periodically calibrated using the Ag $3d_{5/2}$ (368.3 eV) and Au $4f_{7/2}$ (84.0 eV) lines. A general spectrum was performed in order to know what elements were present on the specimen surface, and high resolution spectra were performed to determine the amount and the combination state (valence) of each element.

XPS analyses were normally repeated two or three times, verifying reasonable reproducibility. The atomic percentages of the chemical elements and species present on the specimen surface were obtained from the area of the different components used in the fitting of the high resolution spectrum.

2.4 Scanning electron microscopy

SEM was used to examine sections of the coating parallel to the surface plane. This sections were obtained by polishing with 1 μm diamond paste and finishing with magnesia. The polished specimens were etched in a 10% phosphoric acid solution for 30 s, washed in alcohol in an ultrasonic bath, coated with gold or platinum in vacuum, and studied in a JEOL JSM 6500F scanning electron microscope. The gold or platinum coatings reduce the effect of charging of the surface by the electron beam and improve the image contrast quality.

2.5 Characterisation of anodic layers by EIS

Impedance diagrams were recorded for the sealed and unsealed anodised specimens, immediately after anodising

Table 1 Chemical composition of aluminium alloys (weight percentage)

Specimen	Si	Fe	Cu	Mn	Mg	Cr	Zn	Ti
Pure Al	0.080	0.290	0.003	0.003	0.006	–	0.040	0.012
Al–Cu	0.370	0.340	4.040	0.630	0.600	0.010	0.050	0.050
Al–Mg–Si	0.880	0.360	0.040	0.470	0.800	0.003	0.040	0.060
Al–Mg	0.090	0.260	0.001	0.110	2.900	–	0.022	0.004

and sealing and after different ageing times. A surface area of 1 cm^2 was exposed to the test solution, applying a frequency range from 1 mHz to 100 kHz and using the same equipment and test cell as previously reported [8, 16, 17].

Numerous authors have used EIS to characterise the barrier and porous layers resulting from the anodising of aluminium and its alloys [2–10]. Different equivalent circuits have been proposed to simulate the behaviour of anodised aluminium [2–4]. The authors have demonstrated a very satisfactory agreement between experimental and fitted values with the EC shown in Fig. 1, whose elements represent the different structural peculiarities of anodic coatings [8]. R_p and R_b are the resistances of the porous and barrier layers and C_p and C_b the associated non-ideal capacitances or CPE. C_{pw} represents the non ideal capacitance of the hexagonal cell walls; because of his very high value, the parallel resistance associated with this last element does not significantly influence the system response, so it has been excluded from the EC. However, other much simpler ECs, initially proposed by Hitzing and Juttner for sealed and unsealed anodic films and reproduced in Fig. 2, yield sufficiently approximate responses for most practical applications, and are taken as the essential basis for the estimates made in the present research.

Figure 2 shows the typical impedance diagrams of an anodic film in unsealed state and another after 45 min of traditional hydrothermal sealing (2.5 min/μm of thickness) in boiling deionised water. It can be seen that in a wide frequency range the impedance of the sealed and unsealed anodic films differs by 2–3 orders of magnitude, making EIS a very sensitive tool to discern sealing quality or to detect changes in the characteristics of the barrier and porous layers. This figure also shows, in schematic form, how the capacitance of the barrier and porous layers, C_b and C_p, can be estimated by extrapolation of the straight line regions to the angular frequency $\omega = 1$, and how the

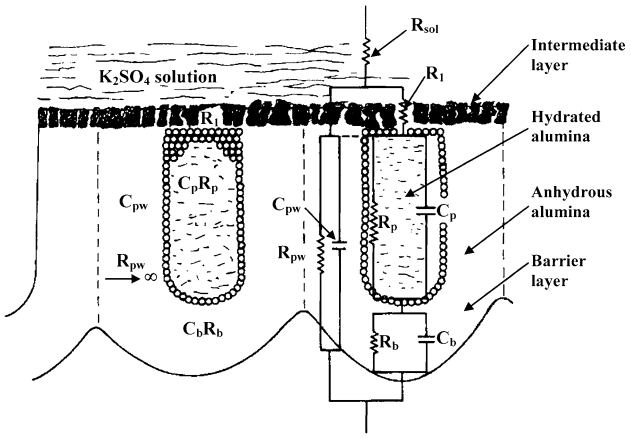

Fig. 1 Scheme of structure of an anodised aluminium oxide film. The proposed EC is superimposed

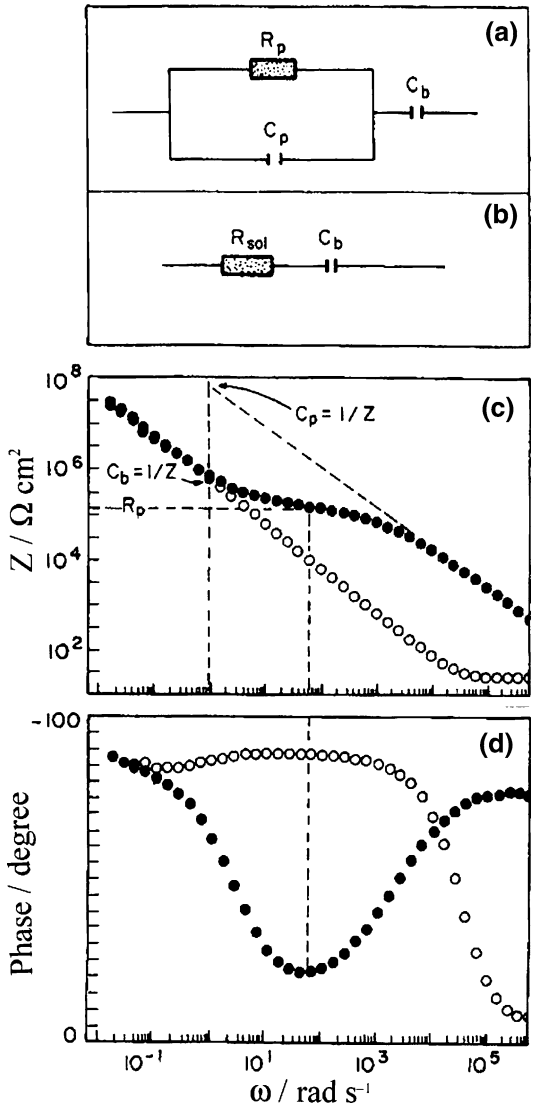

Fig. 2 Simplified CEs for sealed (**a**) and unsealed (**b**) anodic films, and typical impedance diagrams for a correctly sealed (●) and unsealed (○) anodic film (**c** and **d**)

porous layer resistance R_p can be estimated from the impedance value corresponding to the minimum phase angle θ [8].

2.6 Other tests

The thickness of the anodic coatings (between about 5 and 35 μm) was determined instrumentally using equipment based on Foucault currents.

Gravimetry was used to determine the porosity of the anodic coatings and the film formation efficiency. For this purpose, specimens were weighed immediately after surface preparation, prior to anodising, and after each of the subsequent processes of anodising, sealing, and removal of the coatings in boiling phosphochromic mixtures [27].

3 Experimental results

3.1 XPS analysis of surface oxides

Tables 2, 3 and 4 show the elemental compositions obtained by XPS on the aluminium alloy surfaces after etching in a soda solution prior to anodising, immediately after the anodising operation, and after the sealing process in boiling deionised water, respectively. Attention is drawn to the absence of significant amounts of magnesium or copper, the main alloying elements of the Al–Cu, Al–Si–Mg and Al–Mg alloys, when in the oxides from the thermomechanical obtainment treatment the Mg/(Mg + Al) atomic ratios yielded by XPS reach values of the order of 0.20, practically irrespective of their content in the bulk alloy [28].

Figures 3a–d show the high resolution XPS spectra for Al2p obtained on the original aluminium alloy surfaces after etching. Each spectrum contains two components which can be associated with the presence of metallic Al (72.5 eV) and oxidised Al (75.00 eV).

Table 2 Atomic percentages observed by XPS on the outer surface of the various alloys after etching prior to anodising and after 10 min of argon ion bombardment

Specimen	% O	% Al	% Mg	% Cu	O/Al
Pure Al	60	40	0	0	1.5
Al–Cu	60	40	0	1	1.5
Al–Mg–Si	61	39	0	0	1.56
Al–Mg	58	38	0	0	1.53

Table 3 Atomic percentages observed by XPS on the outer surface of the various alloys after the anodising operation

Specimen	% O	% Al	% S	O/Al	Most probable compounds
Pure Al	66	32	2	2.1	AlOOH
Al–Cu	66	32	2	2.1	AlOOH
Al–Mg–Si	64	33	3	1.9	AlOOH
Al–Mg	64	34	2	1.9	AlOOH

Table 4 Atomic percentages observed by XPS on the outer surface of the various alloys after anodising and sealing operations

Specimen	% O	% Al	% S	O/Al	Most probable compounds
Pure Al	73	27	0	2.7	$Al(OH)_3$
Al–Cu	73	27	0	2.7	$Al(OH)_3$
Al–Mg–Si	73	27	0	2.7	$Al(OH)_3$
Al–Mg	74	26	0	2.8	$Al(OH)_3$

With regard to the anodised specimens, the most notable differences are seen between the O/Al ratios of the sealed and unsealed oxides. Figures 4a–d show the high resolution XPS spectra for O1s obtained on the original surface of the anodised pure Al, Al–Cu, Al–Si–Mg and Al–Mg specimens. The two most intense components in the O1s spectra appear at binding energies of 531.0 and 532.0 eV, associated with the presence of oxygen in the form of oxide and OH^-, respectively. Another less intense component appears at a binding energy of 533.5 eV, which may be associated with the presence of water.

Figures 4e–h display the XPS spectra for O1s obtained on the sealed specimens. The intensities of the component associated to the presence of OH^- increase significantly, compared to those observed on the unsealed anodised specimens (Fig. 4a–d), and the intensity of the component associated to the presence of water also increases, above all on the surfaces of the Al–Cu (Fig. 4f) and Al–Mg (Fig. 4h) specimens. The O/Al ratios (Table 4) are close to three, corresponding to trihydrated alumina $Al(OH)_3$, which may suggest that during the sealing process and subsequent ageing of the anodic layer, interaction between water and the cell walls may lead to the formation of bayerite ($Al_2O_3 \cdot 3H_2O$).

Although the procedure is not described, it is noted that XPS was also used to determine the thickness of the passivating layers formed after chemical etching in the aqueous solution of sodium hydroxide, estimating values of 2.2 nm, 2.3 nm, 3.0 nm and 3.8 nm for the pure Al and the Al–Si–Mg, Al–Mg and Al–Cu alloys, respectively (Table 5) [28].

3.2 Characteristics of anodic layers determined by gravimetry

Table 5 lists a series of macroscopic parameters that determine the quality of the anodic films, or at least their quality prior to the sealing process. The cause-effect temporal sequence may be as follows:

(a) The perfectness of the passivating layer influences the mass losses during etching in NaOH ($-\Delta m$) and determines the perfectness of the barrier and porous layers with a mass increase, during anodising, which is greater the more compact they are.
(b) For the same thickness, smaller mass increases during anodising correspond to less compact oxide films, i.e. with greater porosity.
(c) This parameter determines the mass gain in sealing, if this is prolonged sufficiently for the pores to become saturated.
(d) The greater the porosity, the greater the dissolution of the anodic film in the anodising bath, which is pro-

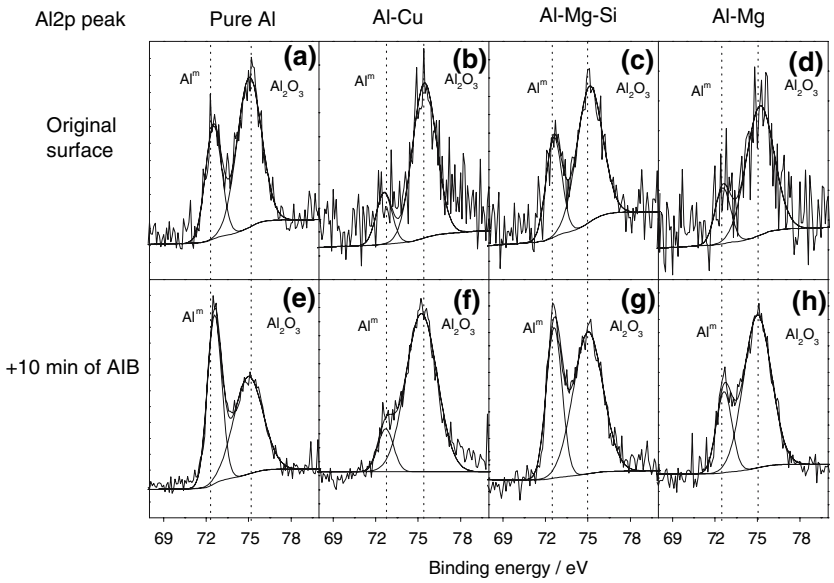

Fig. 3 Evolution of high resolution XPS spectra for Al2p corresponding to pure Al, Al–Cu, Al–Si–Mg and Al–Mg specimens after etching (**a**–**d**) and effect of argon ion bombardment (**e**–**h**)

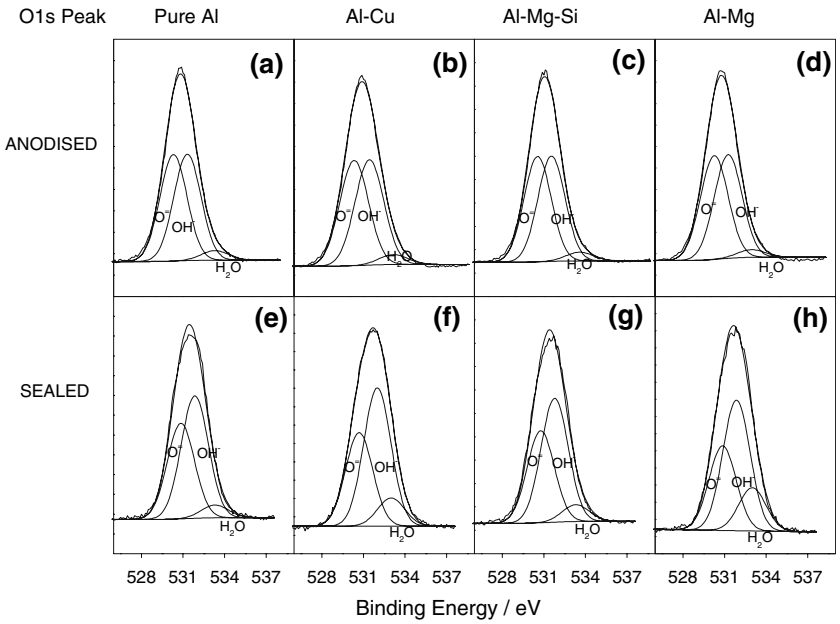

Fig. 4 High resolution XPS spectra for O1s obtained on original surface of anodised pure Al, Al–Cu, Al–Si–Mg and Al–Mg (**a**–**d**) and after sealing (**e**–**h**)

Table 5 Different parameters of the anodic films obtained, by interpolation of the results, for layers of 20 μm thickness. (Δm = mass increase in the different treatments; R = coating ratio)

Alloy	–Δm NaOH (mg) (5 min)	Δm anodising (mg)	Porosity (%)	Δm sealing (mg)	–Δm H_2SO_4 (mg)	R	Pass. layer thickness (nm)
Pure Al	140	120	15	35	50	1.39	2.2
Al–Si–Mg	146	150	13	29	75	1.42	2.3
Al–Mg	205	100	25	50	190	1.20	3.0
Al–Cu	224	–190	40	68	230	0.74	3.8

portional to its surface development, since the composition of the unsealed anodic oxides differs little from one alloy to another (Table 3).

(e) The smaller mass increase during anodising, together with greater dissolution of the anodic film in the anodising bath, explains why the anodic oxide for-

mation efficiency deteriorates progressively from pure aluminium and Al–Si–Mg, to Al–Mg and Al–Cu.

The consequence of all the gravimetric checks is the determination of a series of parameters that are always more unfavourable in the case of Al-Mg and above all in the case of Al–Cu than in the cases of pure Al and Al–Si–Mg.

3.3 Determination of electrochemical parameters by EIS

Figure 5 shows impedance diagrams for the four tested aluminium alloys immediately after sealing. The R_t values deducible from the Nyquist plots (Fig. 5a), which correspond with the porous layer resistance values R_p, show a maximum value for Al–Si–Mg followed by the value corresponding to pure Al, somewhat less for the case of Al–Mg, perhaps as a consequence of the greater porosity of the oxide (Table 5), and much lower for Al–Cu, to the point that, in order to appreciate its R_p, it would be necessary to make a new representation on a scale 10 times smaller. This impediment is overcome in the Bode diagrams thanks to their logarithmic scale (Fig. 5b). The quasi horizontal sections, defined by the resistive control due to the R_p values, show that the transfer resistance of Al–Cu is one order of magnitude smaller than that corresponding to the other alloys. These results may be an effect of the greater porosity of the anodic films developed on Al–Cu, and may explain the much lower efficiency in the anodising process (parameter R in Table 5) or may be a consequence of this. Comparison with the curve corresponding to an unsealed anodic film allows enormous differences to be seen compared to the typical diagrams of sealed oxides.

Figure 6, which displays the responses of recently obtained unsealed anodic films, shows practically identical behaviour with all the materials except for Al–Cu. The capacitive control attributable to the barrier layer extends across the entire frequency range, without significant differences between the results for pure Al, Al–Si–Mg or Al–Mg. The diagram for Al–Cu is, however, substantially different, with Z values that are one order of magnitude lower at medium and low frequencies and which coincide at high frequencies. The control continues to be capacitive but shifts from capacitance values of around 1 μF cm^{-2} to values which are some 10 times higher, characteristic of passivating films that are much thinner than the barrier layers.

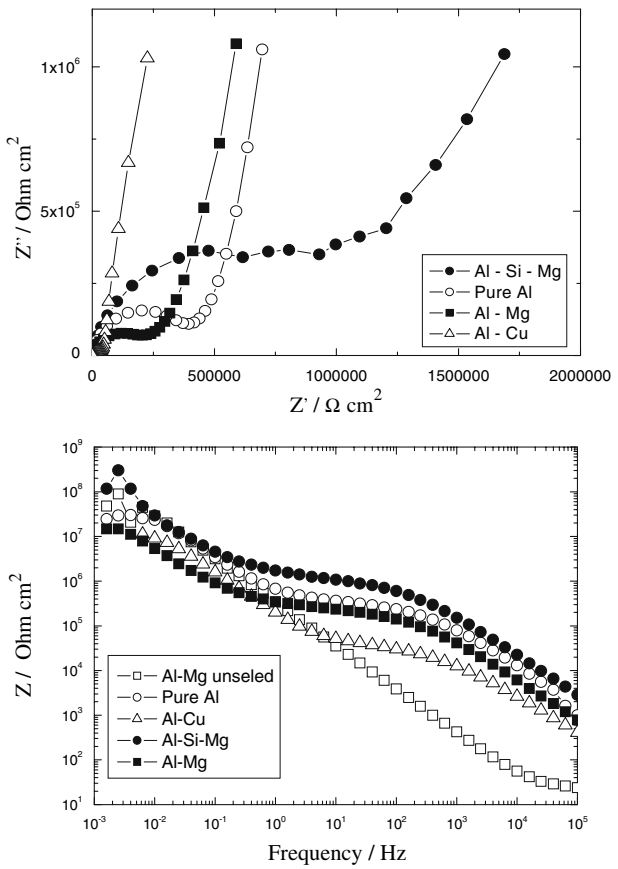

Fig. 5 Impedance diagrams (Nyquist and Bode) for anodic films of intermediate thickness recently obtained and sealed. For comparative purposes, the diagram for the unsealed Al–Mg alloy is included

Table 6 Data for recently sealed anodic films (exposure time 0 months)

Alloy	θ min	R_p (kΩ cm^2)	C_b (μF cm^{-2})	C_p (nF cm^{-2})
Pure Al	–15.1	432	1.04	8
Al–Si–Mg	–20.1	1280	0.42	3.2
Al–Mg	–29.1	251	1.8	10.2
Al–Cu	–24.6	37	0.96	71

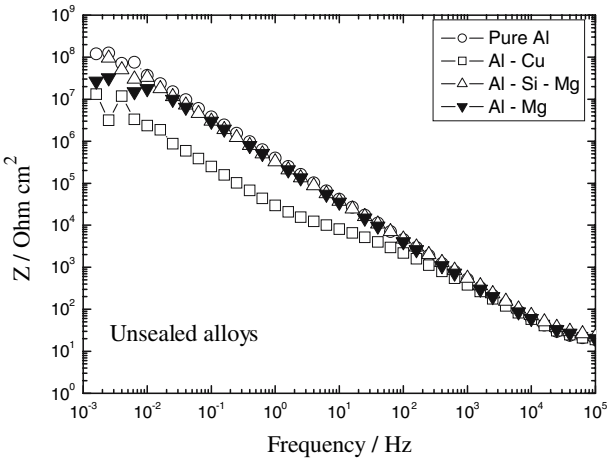

Fig. 6 Bode diagrams for unsealed anodic films, of intermediate thickness, formed on the four tested alloys

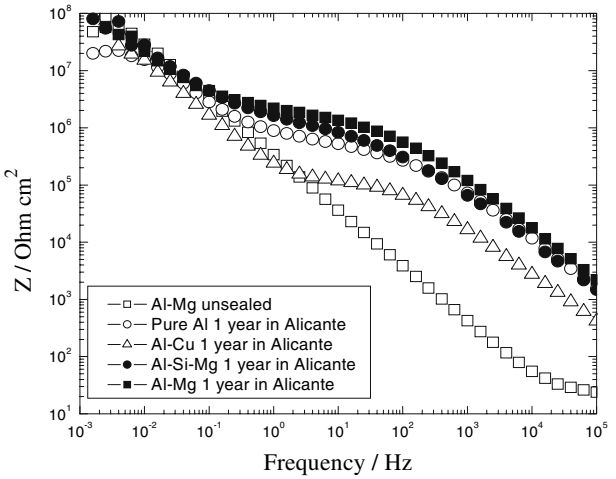

Fig. 7 Bode diagrams for sealed anodic films, of intermediate thickness, formed on the four tested alloys, after one year of exposure to the Alicante atmosphere. For comparative purposes, the typical diagram for an unsealed anodic film is included

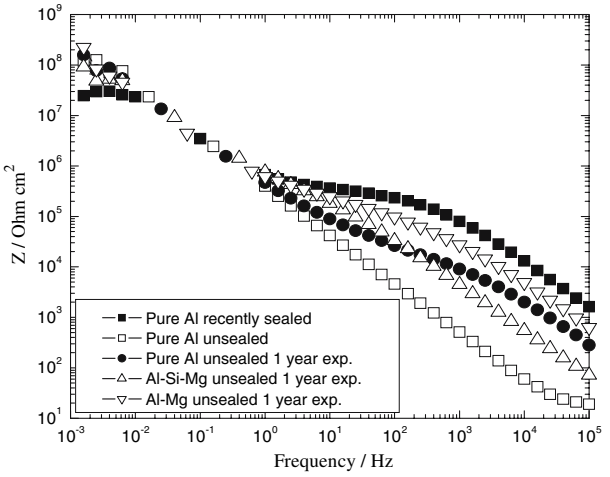

Fig. 8 Due to a slow self-sealing process, the unsealed anodic films exposed for 12 months at the Alicante atmospheric testing station show intermediate impedance diagrams between those typical for an unsealed and a correctly sealed anodic film

Figure 7 presents a Bode diagram for the four sealed alloys after one year of exposure in the marine atmospheric testing station at Alicante. In all cases an improvement of the quality of anodic films can be seen, which is reflected in an increase in the porous layer resistance values R_p. Again with the exception of the Al–Cu alloy, the other three alloys show similar behaviour. An appreciable increase in R_p also takes place on the Al–Cu alloy, but it nevertheless continues to be much lower than the R_p of the pure Al, Al–Si–Mg and Al–Mg.

This progressive improvement in the anodic layer quality indices with ageing may be verified by comparing the R_p, C_p and C_b values corresponding to the sealed anodic films immediately after obtainment and after one year of exposure to the atmosphere as presented in Tables 6 and 7, respectively. The values of the various parameters are estimated from the impedance diagrams using the procedures schematised in Fig. 2.

The unsealed anodic films exposed to the atmosphere reveal the self-sealing capacity that has been determined in previous research with coatings developed on aluminium of commercial purity (1050 alloy) [20–24]. Figure 8 shows that after one year of exposure in the Alicante atmosphere, intermediate impedance diagrams between unsealed and correctly sealed oxides are obtained. The degree of self-sealing has very probably not progressed more due to the extremely dry conditions prevailing in Spain during the exposure time (June 2004–2005). In humid environments self-sealing is capable of producing sealing qualities that exceed industrial requirements in much shorter time periods, approximately two months [24]. Figure 9 shows the verification of this process in the case of the Al–Mg alloy exposed for 2 months in a humidity cabinet, which is also representative of the behaviour of pure Al and of the Al–Si–Mg alloy.

Figures 10a, b and c, which display impedance diagrams for the three alloys that develop good quality anodic films,

Table 7 Data for anodic films exposed for 12 months in the natural testing site at Madrid

Alloy	θ (min)	R_p (kΩ cm^2)	C_b (μF cm^{-2})	C_p (nF cm^{-2})
Pure Al	–21.5	2206	0.24	3.3
Al–Si–Mg	–28.2	3530	0.48	5.6
Al–Mg	–19.1	890	1.80	12.5
Al–Cu	–22.2	118	0.91	59

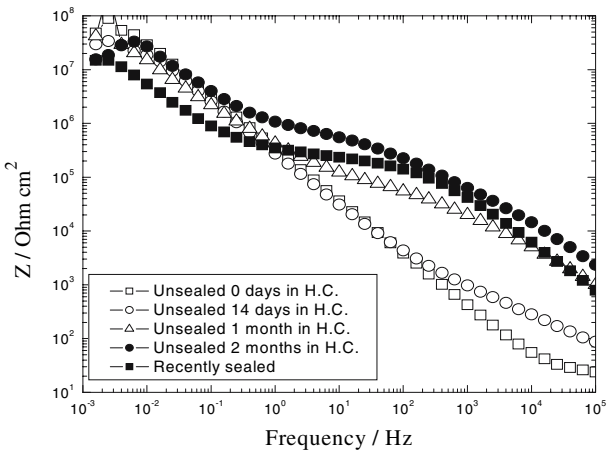

Fig. 9 Rapid evolution of self-sealing process in the case of Al–Mg alloy exposed for 2 months in humidity cabinet. After this time the impedance diagram is characteristic of sealed anodic films

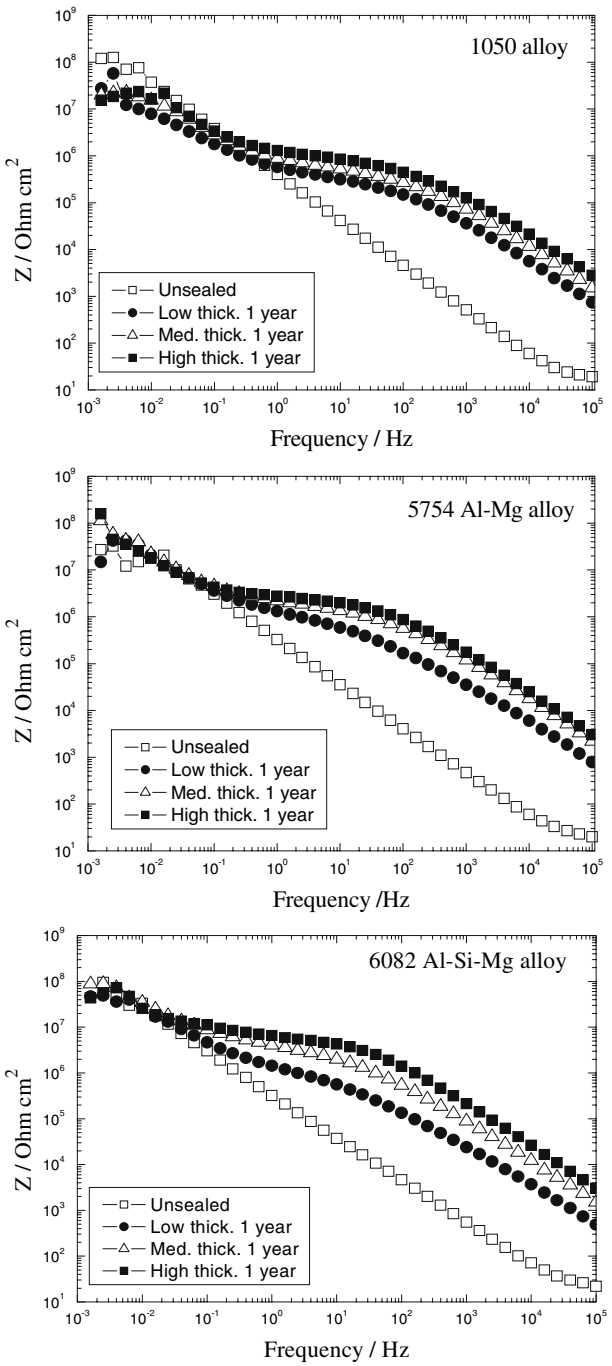

Fig. 10 Comparison of impedance diagrams, for the three tested anodic film thicknesses, of pure Al, Al–Mg and Al–Si–Mg specimens exposed for one year to the Madrid atmosphere

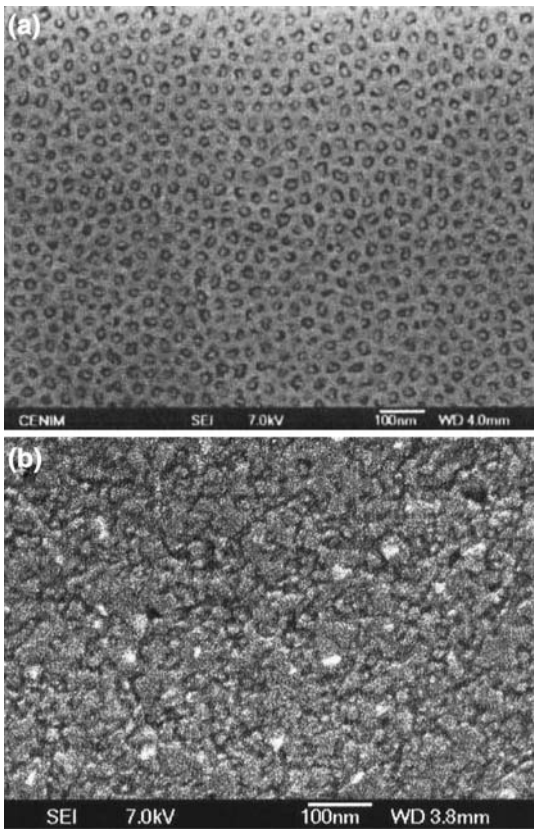

Fig. 11 SEM micrographs of sealed anodic films formed on pure Al (**a**) and on the Al–Cu alloy (**b**). Scale dimensions are 100 nm

show qualitatively and quantitatively similar responses for coatings of low, medium and high thicknesses in all cases. At high frequencies, sections of parallel capacitive control are obtained which, by extrapolation to the angular frequency $\omega = 1$, yield porous layer capacitance values (C_p) that are inversely proportional to the thickness, being practically the same for all three alloys.

With the scanning electron microscope, observations were made of sections parallel to the surface plane of the anodic films formed on the various alloys. The results are very similar for pure Al, Al–Mg and Al–Si–Mg, revealing a pore network that follows the well-known hexagonal distribution, as can be seen in Fig. 11a for a sealed anodic layer formed on pure Al. The attempt to anodise the Al-Cu alloy results in the formation of oxide layers in which it is impossible to discover a regular porous structure, as is verified in Fig. 11b. Their appearance is reminiscent of an earthy agglomerate with numerous grooves and irregularities.

4 Discussion

4.1 Chemical composition of surface oxides

Attention is drawn to the similarity of the composition of the surface oxide layers on all the alloys, with regard to both the passivation layer formed after etching (Table 2) and the anodic films formed both before (Table 3) and after (Table 4) the sealing operation. In no case are significant proportions of the main alloying elements: Mg, Cu or Si, detected. In the passivating layers the O/Al ratio is very

close to 1.5, so they must comprise essentially Al_2O_3. The O/Al ratio is around 2 in the anodic layers (Table 3), and so the most probable compound is the monohydrate AlOOH ($Al_2O_3 \cdot H_2O$), which highlights the capacity of the anodic oxides to react with environmental humidity, at least in their surface layers. The participation of 2% S comes from the known sulphate ion pollution of the anodising bath. The sealing process, with the dissolution of alumina from the cell walls and the formation and precipitation of hydrates inside the pores, leads to an O/Al ratio $\approx$ 2.7 (Table 4), an intermediate value between the alumina of the pore walls and the trihydrate of the pore interior, $Al(OH)_3$ ($Al_2O_3 \cdot 3H_2O$).

All the signs seem to be that the great similarity between the chemical compositions of the anodic films developed on the various alloys would justify similar responses by these films. Therefore, the significant differences shown by Al–Mg compared to pure Al and Al–Si–Mg, and the radically different behaviour of Al–Cu, must be due to other causes.

4.2 Macroscopic characteristics of the anodic films

The passivating layers formed as a result of etching prior to anodising have a thickness that varies between 2.2 nm for pure Al and the 3.8 nm estimated for Al–Cu (Table 5). The more network defects that the passivating films have, the easier the egress of Al^{3+} and the O^{2-} ingress across the pre-existing oxide film, the greater the thickness achieved, and the lower its protective power. These imperfections in the passivating oxide are transmitted in some way to the anodic oxides, and so the porosity of the anodic films on pure Al is practically identical to that found on Al–Si–Mg, considerably lower than on Al–Mg, and only approximately one third of that shown by Al–Cu (Table 5). In turn, the porosity controls the amount of attack of the oxides in the anodising bath, and so an additional amount of aluminium is consumed to obtain the same anodic film thickness, which means that the anodising efficiency (coating ratio, R) is lower the greater the porosity. Moreover, the lower the protective power of the surface oxides, the greater the expectable direct attack of the metallic substrate which, in turn, would contribute to a supplementary drop in the anodising efficiency in the case of Al–Mg, but above all in the case of Al–Cu, as is witnessed by the data in Table 5.

Curiously the XPS technique demonstrates the similarity of the chemical compositions of all the anodic films (Tables 3 and 4). The cause of the striking differences between Al–Cu and the Al alloys that are capable of developing quality anodic films lies in the microstructural characteristics of these oxides which are built with the same elements and in the same proportions. Figures 11a and b show totally different microstructural assemblies. A regular porous structure with hexagonal cells in a honeycomb arrangement (Fig. 11a), described decades ago as being characteristic of the anodic films formed on aluminium and its alloys, revealed by SEM in an anodic film formed on pure Al (Fig. 11a) but which is perfectly representative of the anodic films formed on Al–Mg and Al–Si–Mg, and an irregular "earthy" structure with innumerable grooves and microdefects (Fig. 11b), which corresponds to anodic layers of low thickness formed on Al-Cu. As the thickness of the latter grows, the defects and the disorder multiply, leading to powdery products that collapse under the slightest abrasion. This radically different microstructure may be the main cause of the great differences in quality between anodic oxides on Al–Cu and on the rest of the alloys.

4.3 Determination of electrochemical parameters of anodic films

Sealing plugs the mouth of the pores and represents resistance to the passage of current which may be quantified either by the semicircle in Nyquist diagrams (Fig. 5a) or by the impedance of the almost horizontal section in Bode diagrams (Figs. 2c, 5b). This resistance of recently sealed porous layers (R_p) is seen to be maximum for the Al–Si–Mg alloy, somewhat lower for pure Al, a little lower for Al–Mg, and approximately one order of magnitude lower for Al–Cu. The greater porosity of the anodic layers on Al–Mg, and above all on Al–Cu (Table 5), may be the main cause of the drop in R_p, since the pore fill material presents far lower resistivity than the hexagonal cell walls.

In contrast, in the diagrams of the unsealed anodic films only the straight line section imposed by the C_b value is defined, which is common for pure Al, Al–Mg and Al–Si–Mg (Fig. 6). Again the Al–Cu alloy presents singular behaviour, exhibiting one section at high frequencies, which is confused with that of the other alloys, and another at medium-low frequencies, which parts from the common behaviour. Bearing in mind the expression that defines capacitance:

$$C = \varepsilon_0 \cdot \varepsilon \cdot S/\delta \quad (1)$$

the initial common straight line section would indicate barrier layers of similar electrical permittivities, ε, since their thickness, δ, is the same, approximately 150 Å, given that they have been produced under an identical voltage of 15 V, and in the case of those anodised in sulphuric acid the thickness of the barrier layers is around 10 Å V^{-1} [29]. At medium and low frequencies another straight line section is defined on Al–Cu with a similar slope but with Z values one order of magnitude

lower, leading to capacitance values 10 times greater, typical of passivating layers, with thicknesses of approximately 2–3 nm (20–30 Å) (Table 5). The barrier layer on Al–Cu is probably perforated by numerous defects with its base protected by passivating layers.

The final stage of the complex sealing mechanism, ageing, continues for months and years, with progressive increase in R_p, reflected by the shifting of the central section of the Bode diagrams towards higher Z values (Fig. 7, Tables 6 and 7), which, according to the literature, is equivalent to a progressive improvement in anodic film quality [2, 24].

The progressive improvement of anodic films also takes place in unsealed anodic layers, slowly in atmospheric exposure (Fig. 8) and much faster in a humidity cabinet (Fig. 9). The behaviour verified in a wide variety of atmospheres for pure Al anodic layers [20–24] is thus repeated in Al–Mg and Al–Si–Mg, which exhibit entirely comparable self-sealing and ageing processes. Even the defective anodic films on Al–Cu show a significant increase in R_p, though greatly different to the R_p values determined on the other alloys (Fig. 7, Tables 6 and 7).

Considering that on specimens of intermediate thickness the porous layer is situated very approximately around 15 μm, as has repeatedly been verified by various procedures, and that the C_p estimated from the impedance diagrams is $\approx 5 \times 10^{-9}$ F cm^{-2}, with the dielectric constant of the vacuum being $\varepsilon_0 = 8.854 \times 10^{-14}$ F cm^{-1}, expression (1) yields a permittivity or relative dielectric constant of $\varepsilon = 85$ for alumina, much higher than the generally accepted value of $\varepsilon = 10$ [4]. In contrast, for the barrier layer, with a capacitance of $C_b \approx 10^{-6}$ F cm^{-2} and a thickness of around 15 nm, a permittivity of $\varepsilon = 17$ is obtained, almost twice that proposed for alumina in the table of constants. It may be considered that contamination of the anhydrous alumina by S from the $SO_4^{=}$ anion (Table 3) multiplies its permittivity by 2, something that is perfectly credible. The very high value found for the porous layer, $\varepsilon = 85$, is attributable to the characteristics of the pore infill, since the permittivity of the hexagonal cell walls must be the same as that of the barrier layer.

This leaves the calculation of the barrier layer resistance, R_b, as the final component of the EC. Given that at the minimum frequency used in the obtainment of the impedance diagrams (1 mHz), and except for unusual cases, no other new zone of resistive control imposed by R_b is insinuated (Figs. 5–10), despite reaching Z values of $\geq 10^8$ Ω cm^2, one must conclude that the barrier layer resistance exceeds this value. Accepting this threshold value and the thickness of 15 nm for the barrier layer, this would give a resistivity for this layer of approximately $\rho_b \geq 1 \times \Omega\ \text{cm}^2/15 \times 10^{-7}\ \text{cm} \geq 6.7 \times 10^{13}\ \Omega\ \text{cm}$, which acceptably agrees with the value of 10^{14} Ω cm indicated for alumina by the Goodfellow catalogue [30].

In contrast, very different values are reached when basing the calculations on the porous layer resistance, R_p, whose measurement from the impedance diagrams offers no doubt. With R_p values of around 500,000 Ω cm^2 for recently sealed anodic layers (Table 6) of approximately 15 μm in thickness, it is possible to estimate a $\rho_p = 500{,}000\ \Omega\ \text{cm}^2/15 \times 10^{-4}\ \text{cm} = 3.3 \times 10^8\ \Omega\ \text{cm}$, some five orders of magnitude lower than the previously calculated ρ_b. The pore fill possesses a comparatively very high electrical conductivity compared to the conductivity of the cell walls and the barrier layer, no matter how much hydration has progressed and the remains of intercrystalline water have disappeared. With the ageing process ρ_p increases progressively [8], but always remains several orders of magnitude below ρ_b.

5 Conclusions

1. XPS reveals a notably lower O/Al ratio in unsealed anodic layers than in sealed layers, but in both cases the composition is practically the same for all four studied alloys, which means that the differences in behaviour must be due to other causes.
2. All the parameters that macroscopically define anodic film quality, i.e. their porosity, R_p, or the coating ratio, are very similar on pure Al and Al–Si–Mg, somewhat lower on Al–Mg, and very deficient in the case of the Al–Cu alloy anodised in sulphuric acid.
3. The impedance diagrams for recently obtained anodic films reveal a slightly lower R_p (quality) on the Al–Mg alloy than on pure Al and Al–Si–Mg, and a very deficient value in the case of the Al–Cu alloy.
4. Ageing gradually improves the quality indices of anodic films on Al–Si–Mg and Al–Mg, as has previously been verified with pure Al. For exposure times of more than one year the electrical characteristics of the anodic layers estimated by EIS are practically the same on these three alloys, but continue to be very deficient in the case of Al–Cu.
5. Unsealed anodised aluminium undergoes a self-sealing process at ambient temperature in all types of atmospheres, which is faster the greater the precipitation and the higher the environmental relative humidity.
6. With a sufficiently long self-sealing time the impedance diagrams evolve, in all types of atmospheres, from diagrams characteristic of unsealed anodic films to those typical of correctly sealed anodic films.
7. All the quality indices of the unsealed anodic films improve with self-sealing/ageing, and can even exceed industrially established requirements.

Acknowledgements This work was supported by the Comisión Interministerial de Ciencia y Tecnología (CICYT) of Spain within the framework of Project MAT2003–02217.

References

1. Brace AW (1979) The technology of anodizing aluminium. Tecnicopy Ltd. Stonenhouse, Gloucestershire, England, pp 1–19
2. Hoar TP, Wood GC (1962) Electrochim Acta 7:333
3. Hitzing J, Juttner K, Lorenz WJ, Paatsch W (1986) J Electrochem Soc 103:887
4. Hitzing J, Juttner K, Lorenz WJ, Paatsch W (1984) Corros Sci 24:945
5. Mansfeld F (1988) Corrosion 44:856
6. Van der Linden B, Terryn H, Vereecken J (1990) J Appl Electrochem 20:798
7. González JA, López V, Otero E, Bautista A (2000) J Electrochem Soc 147:984
8. González JA, López V, Bautista A, Otero E, Nóvoa XR (1999) J Appl Electrochem 29:229
9. Suay JJ, Jiménez E, Rodríguez T, Aviv K, Saura JJ (2003) Corros Sci 45:611
10. Celati N, Sainte Catherine MC, Keddam M, Takenouti H (1995) Mater Sci Forum (192–194):335
11. Wood GC (1959) Trans Inst Metal Finish 36:220
12. Wefers K (1973) Aluminium 49(8):553 and 49(9):622
13. Shimizu K, Kobayashi K, Thompson GE, Wood GC (1985) J Appl Electrochem 15:781
14. Thompson GE, Furneaux RC, Wood GC (1978) Corros Sci 18:481
15. Thompson GE, Wood GC (1981) Nature 290:230
16. Lizarbe R, González JA, Otero E, López V (1993) Aluminium 69:548
17. López V, González JA, Bautista A, Otero E, Lizarbe R (1998) Corros Sci 40: 693
18. López V, Bartolomé MJ, Escudero E, Otero E, González JA (2006) J Electrochem Soc 153(3):B75
19. González JA, Feliu Jr S, Bautista A, Otero E, Feliu S (1999) J Appl Electrochem 29:845
20. González JA, López V, Otero E, Bautista A, Lizarbe R, Barba C, Baldonedo JL (1997) Corros Sci 39:1109
21. González JA, Morcillo M, Escudero E, López V, Otero E (2002) J Coat Technol 153:225
22. López V, González JA, Otero E, Escudero E, Morcillo M (2002) J Coat Technol 153:235
23. López V, Escudero E, González JA, Otero E, Morcillo M (2004) Rev Metal Madrid 40:270
24. Escudero E, Bartolomé MJ, López V, Simancas J, González JA, Morcillo M, Otero E (2005) Rev Metal Madrid 41:133
25. Huttunen-Saarivirta E, Tiainen T (2004) Mater Chem Phys 85:383
26. Páez MA, Foong TM, Ni CT, Thompson GE, Shimizu K, Habazaki H, Skeldon P, Word GC (1996) Corros Sci 38:59
27. Standard UNE-EN 12373–2:1999, Aluminio y aleaciones de aluminio. Anodización. Parte 2: Determinación de la masa por unidad de superficie de los recubrimientos anódicos de óxido. Método gravimétrico
28. Feliu Jr S, Bartolomé MJ (2007) Surf Interface Anal 39:304
29. Keller F, Hunter MS, Robinson DL (1953) J Electrochem Soc 100(9):411
30. Goodfellow Catalogue (1996/7):409